Biomedical Optics EXPRESS

A 5-mm piezo-scanning fiber device for high speed ultrafast laser microsurgery

Onur Ferhanoglu, Murat Yildirim, Kaushik Subramanian, and Adela Ben-Yakar*

Department of Mechanical Engineering, The University of Texas at Austin, Austin, Texas 78712, USA
ben-yakar@mail.utexas.edu

Abstract: Towards developing precise microsurgery tools for the clinic, we previously developed image-guided miniaturized devices using low repetition rate amplified ultrafast lasers for surgery. To improve the speed of tissue removal while reducing device diameter, here we present a new 5-mm diameter device that delivers high-repetition rate laser pulses for high speed ultrafast laser microsurgery. The device consists of an air-core photonic bandgap fiber (PBF) for the delivery of high energy pulses, a piezoelectric tube actuator for fiber scanning, and two aspheric lenses for focusing the light. Its inline optical architecture provides easy alignment and substantial size reduction to 5 mm diameter as compared to our previous MEMS-scanning devices while realizing improved intensity squared (two-photon) lateral and axial resolutions of 1.16 µm and 11.46 µm, respectively. Our study also sheds light on the maximum pulse energies that can be delivered through the air-core PBF and identifies cladding damage at the input facet of the fiber as the limiting factor. We have achieved a maximum energy delivery larger than 700 nJ at 92% coupling efficiency. An in depth analysis reveals how this value is greatly affected by possible slight misalignments of the beam during coupling and the measured small beam pointing fluctuations. In the absence of these imperfections, self-phase modulation becomes the limiting factor for the maximum energy delivery, setting the theoretical upper bound to near 2 µJ for a 1-m long, 7-µm, air-core PBF. Finally, the use of a 300 kHz repetition rate fiber laser enabled rapid ablation of 150 µm x 150 µm area within only 50 ms. Such ablation speeds can now allow the surgeons to translate the surgery device as fast as ~4 mm/s to continuously remove a thin layer of a 150 µm wide tissue. Thanks to a high optical transmission efficiency of the in-line optical architecture of the device and improved resolution, we could successfully perform ablation of scarred cheek pouch tissue, drilling through a thin slice. With further development, this device can serve as a precise and high speed ultrafast laser scalpel in the clinic.

OCIS codes: (170.1020) Ablation of tissue; (140.7090) Ultrafast lasers; (180.4315) Nonlinear microscopy; (170.3890) Medical optics instrumentation; (190.4370) Nonlinear optics, fibers.

References and links

1. A. Vogel and V. Venugopalan, "Mechanisms of pulsed laser ablation of biological tissues," Chem. Rev. **103**(2), 577–644 (2003).
2. M. F. Yanik, H. Cinar, H. N. Cinar, A. D. Chisholm, Y. Jin, and A. Ben-Yakar, "Neurosurgery: functional regeneration after laser axotomy," Nature **432**(7019), 822 (2004).
3. G. M. Kezirian and K. G. Stonecipher, "Comparison of the IntraLase femtosecond laser and mechanical keratomes for laser in situ keratomileusis," J. Cataract Refract. Surg. **30**(4), 804–811 (2004).
4. S. H. Chung and E. Mazur, "Surgical applications of femtosecond lasers," J. Biophotonics **2**(10), 557–572 (2009).
5. D. V. Palanker, M. S. Blumenkranz, D. Andersen, M. Wiltberger, G. Marcellino, P. Gooding, D. Angeley, G. Schuele, B. Woodley, M. Simoneau, N. J. Friedman, B. Seibel, J. Batlle, R. Feliz, J. Talamo, and W. Culbertson,

#206582 - $15.00 USD Received 18 Feb 2014; revised 23 May 2014; accepted 26 May 2014; published 2 Jun 2014

"Femtosecond Laser-Assisted Cataract Surgery with Integrated Optical Coherence Tomography," Sci. Transl. Med. **2**(58), 58ra85 (2010).
6. C. L. Hoy, O. Ferhanoglu, M. Yildirim, K. H. Kim, S. S. Karajanagi, K. M. C. Chan, J. B. Kobler, S. M. Zeitels, and A. Ben-Yakar, "Clinical ultrafast laser surgery: recent advances and future directions," IEEE J. Sel. Top. Quantum Electron. **20**(2), 1–14 (2014).
7. C. L. Hoy, N. J. Durr, P. Chen, W. Piyawattanametha, H. Ra, O. Solgaard, and A. Ben-Yakar, "Miniaturized probe for femtosecond laser microsurgery and two-photon imaging," Opt. Express **16**(13), 9996–10005 (2008).
8. C. L. Hoy, O. Ferhanoğlu, M. Yildirim, W. Piyawattanametha, H. Ra, O. Solgaard, and A. Ben-Yakar, "Optical design and imaging performance testing of a 9.6-mm diameter femtosecond laser microsurgery probe," Opt. Express **19**(11), 10536–10552 (2011).
9. C. Jauregui, J. Limpert, and A. Tünnermann, "High-power fibre lasers," Nat. Photonics **7**(11), 861–867 (2013).
10. M. E. Fermann and I. Hartl, "Ultrafast fibre lasers," Nat. Photonics **7**(11), 868–874 (2013).
11. M. Yildirim, O. Ferhanoglu, J. Kobler, S. M. Zeitels, and A. Ben-Yakar, "Parameters affecting ultrafast laser microsurgery of subepithelial voids for scar treatment in vocal folds," J. Biomed. Opt. **18**(11), 118001 (2013).
12. C. L. Hoy, W. N. Everett, M. Yildirim, J. Kobler, S. M. Zeitels, and A. Ben-Yakar, "Towards endoscopic ultrafast laser microsurgery of vocal folds," J. Biomed. Opt. **17**(3), 038002 (2012).
13. Y. Y. Wang, X. Peng, M. Alharbi, C. F. Dutin, T. D. Bradley, F. Gérôme, M. Mielke, T. Booth, and F. Benabid, "Design and fabrication of hollow-core photonic crystal fibers for high-power ultrashort pulse transportation and pulse compression," Opt. Lett. **37**(15), 3111–3113 (2012).
14. X. Peng, M. Mielke, and T. Booth, "High average power, high energy 1.55 μm ultra-short pulse laser beam delivery using large mode area hollow core photonic band-gap fiber," Opt. Express **19**(2), 923–932 (2011).
15. C. M. Lee, C. J. Engelbrecht, T. D. Soper, F. Helmchen, and E. J. Seibel, "Scanning fiber endoscopy with highly flexible, 1 mm catheterscopes for wide-field, full-color imaging," J. Biophotonics **3**(5-6), 385–407 (2010).
16. J. Xi, Y. Chen, Y. Zhang, K. Murari, M.-J. Li, and X. Li, "Integrated multimodal endomicroscopy platform for simultaneous en face optical coherence and two-photon fluorescence imaging," Opt. Lett. **37**(3), 362–364 (2012).
17. Y. Zhang, M. L. Akins, K. Murari, J. Xi, M.-J. Li, K. Luby-Phelps, M. Mahendroo, and X. Li, "A compact fiber-optic SHG scanning endomicroscope and its application to visualize cervical remodeling during pregnancy," Proc. Natl. Acad. Sci. U.S.A. **109**(32), 12878–12883 (2012).
18. C. J. Engelbrecht, R. S. Johnston, E. J. Seibel, and F. Helmchen, "Ultra-compact fiber-optic two-photon microscope for functional fluorescence imaging in vivo," Opt. Express **16**(8), 5556–5564 (2008).
19. S. D. Senturia, *Microsystem design* (Kluwer academic publishers Boston, 2001).
20. D. A. Cremers and L. J. Radziemski, *Handbook of Laser-Induced Breakdown Spectroscopy* (Jon Wiley & Sons Ltd., 2006).
21. M. C. Teich and B. Saleh, *Fundamentals of photonics* (Wiley Interscience, 1991).
22. B. C. Stuart, M. D. Feit, S. Herman, A. M. Rubenchik, B. W. Shore, and M. D. Perry, "Nanosecond-to-femtosecond laser-induced breakdown in dielectrics," Phys. Rev. B Condens. Matter **53**(4), 1749–1761 (1996).
23. D. Ashkenasi, M. Lorenz, R. Stoian, and A. Rosenfeld, "Surface damage threshold and structuring of dielectrics using femtosecond laser pulses: the role of incubation," Appl. Surf. Sci. **150**(1), 101–106 (1999).
24. R. House, J. Bettis, and A. Guenther, "Surface roughness and laser damage threshold," IEEE J. Quantum Electron. **13**(5), 361–363 (1977).
25. P. Kean, K. Smith, and W. Sibbett, "Spectral and temporal investigation of self-phase modulation and stimulated Raman scattering in a single-mode optical fibre," IEE Proc., Optoelectron. **134**(3), 163–170 (1987).
26. D. G. Ouzounov, F. R. Ahmad, D. Müller, N. Venkataraman, M. T. Gallagher, M. G. Thomas, J. Silcox, K. W. Koch, and A. L. Gaeta, "Generation of megawatt optical solitons in hollow-core photonic band-gap fibers," Science **301**(5640), 1702–1704 (2003).
27. E. J. Seibel and Q. Y. Smithwick, "Unique features of optical scanning, single fiber endoscopy," Lasers Surg. Med. **30**(3), 177–183 (2002).
28. C. L. Hoy, N. J. Durr, and A. Ben-Yakar, "Fast-updating and nonrepeating Lissajous image reconstruction method for capturing increased dynamic information," Appl. Opt. **50**(16), 2376–2382 (2011).
29. L. Zhigilei and B. Garrison, "Mechanisms of laser ablation from molecular dynamics simulations: dependence on the initial temperature and pulse duration," Appl. Phys., A **69**(S1), 75–80 (1999).
30. M. Frentzen, W. Götz, M. Ivanenko, S. Afilal, M. Werner, and P. Hering, "Osteotomy with 80-micros CO_2 laser pulses-histological results," Lasers Med. Sci. **18**(2), 119–124 (2003).
31. T. Chanthasopeephan, J. P. Desai, and A. C. Lau, "Measuring forces in liver cutting: New equipment and experimental results," Ann. Biomed. Eng. **31**(11), 1372–1382 (2003).
32. S. Amini-Nik, D. Kraemer, M. L. Cowan, K. Gunaratne, P. Nadesan, B. A. Alman, and R. J. Miller, "Ultrafast mid-IR laser scalpel: protein signals of the fundamental limits to minimally invasive surgery," PLoS ONE **5**(9), e13053 (2010).
33. M. L. Kaiser, M. Rubinstein, D. E. Vokes, J. M. Ridgway, S. Guo, M. Gu, R. L. Crumley, W. B. Armstrong, Z. Chen, and B. J. Wong, "Laryngeal epithelial thickness: a comparison between optical coherence tomography and histology," Clin. Otolaryngol. **34**(5), 460–466 (2009).

#206582 - $15.00 USD Received 18 Feb 2014; revised 23 May 2014; accepted 26 May 2014; published 2 Jun 2014

1. Introduction

Ablation with ultrafast lasers can provide an unmatched microsurgical precision [1, 2]. However its clinical adoption has been mainly achieved for ophthalmic applications due to the lack of a means to flexibly deliver the laser light to clinical sites in or on the patient [3–6]. To overcome this main technological barrier, we focused our efforts, thus far, on the development of miniaturized fiber probes capable of femtosecond laser microsurgery combined with nonlinear optical imaging. The ability to deliver ultrashort laser pulses with micro-Joule levels of energy through an air-core photonic bandgap fiber (PBF), enabled us to perform precise ablation of individual cancer cells guided with nonlinear imaging using miniaturized probes [7, 8]. By incorporating a scanning mechanism based on microelectromechanical system (MEMS) mirrors, we could also perform a high resolution imaging of tissue intrinsic signals [8]. While, the use of a high repetition rate, 80 MHz, femtosecond laser oscillator was sufficient for imaging, surgery required the use of higher energy pulses from a low repetition rate, 1 kHz, amplified system. However, surgery speeds with such low repetition rate lasers is too slow for clinically relevant procedures and the need for two separate lasers makes the whole system bulky, costly, and complicated.

For clinical use, compact and robust laser systems are desired with high pulse energies and repetition rates to enable image-guided and high speed surgery. Ultrafast fiber lasers offer both high pulse energies and high repetition rates within a compact housing [9, 10]. These features make them ideal for high speed surgery, simultaneously providing imaging capabilities within a single laser unit as demonstrated in our recent benchtop studies [11, 12]. Together with the ability of hollow-core photonic crystal fibers to deliver more than hundreds of micro-Joules of pulse energies [13, 14], it is now feasible to build flexible and potentially hand-held laser scalpels suited for clinical use.

Clinical compatibility also requires further miniaturization of laser scalpel to reach small regions within the body. Relatively large size of packaging and die pieces that accompany MEMS scanners limit further miniaturization of our previously developed MEMS based probes to diameters below 7 – 8 mm. Alternatively, the compact geometry of piezo-scanning based probes has already been exploited in endoscopy for various optical imaging modalities, such as confocal imaging [15], optical coherence tomography [16], and multi-photon imaging [17, 18] to gain access to sites that are otherwise challenging to reach. Additionally, piezo-scanning would enable high optical transmission efficiencies not achievable in MEMS devices with silica based reflective surfaces, which is crucial for high pulse energies during surgery.

To perform high-speed surgery within confined spaces, we have, therefore, designed, developed, and rigorously characterized a new scalpel delivering high-repetition rate laser pulses from an erbium-doped fiber laser (1.5 ps, 300 kHz, 776 nm Discovery, Raydiance Inc.). By incorporating the piezo-scanning mechanism into an in-line optical architecture, we nearly halved the size of the device diameter compared to our previous MEMS based device, reducing its outer diameter to 5 mm. A high optical transmission efficiency further ensured delivery of the high energy pulses with low loss. This paper presents the optical design of this piezo-scanning fiber device, the characterization of its performance, and the high speed microsurgery of a scarred tissue sample. The device acts as a variable-width laser scalpel, with which a surgeon can precisely cut around tumor margins with precision. The scan-width can be altered anywhere from providing narrow cuts (3 – 5 μm in width) to wide cuts (up to 220 μm) for rapidly removing lesions on delicate tissue such as vocal fold ligaments. The paper also presents an in-depth analysis of ultrashort pulse delivery through the air-core PBF and discussion of the associated limitations in delivering maximum pulse energies.

#206582 - $15.00 USD Received 18 Feb 2014; revised 23 May 2014; accepted 26 May 2014; published 2 Jun 2014

2. Results

2.1. Device design and characterization

The selection of critical components for the new 5-mm scalpel involved the consideration of several factors with particular focus on: 1) reducing the device diameter below 5 mm, which is crucial to many clinical applications, 2) using optical components with low spherical aberration and high transmission at low-cost, 3) designing the optical system for a near-diffraction limited spot size through the entire field of view (FOV) while minimizing radius of curvature, 4) tight focusing to deliver high laser fluences for tissue ablation, 5) scanning a FOV of approximately 200 μm × 200 μm, and 6) performing microsurgery at high-speeds.

To maintain the housing diameter below 5 mm, we limited the maximum size of the optical components to 3 mm which meant moving away from the reflective beam steering MEMS scanning mechanisms from our earlier work. In this device, we chose an in-line optical architecture where beam steering is performed by the resonant vibration of a laser delivery fiber via a piezoelectric device. The in-line configuration also increased the transmission efficiency of the device by eliminating the poorly reflecting bare silicon surfaces of our previous MEMS scanning mirrors. Though reflectivity can be enhanced with metal deposition onto the mirror surface, the use of fiber scanning mechanisms instead of a scanning mirror offers the highest efficiency in laser energy delivery in addition to enabling the smallest probe dimensions. For our optical components, we chose off-the-shelf glass molded aspheric lenses. With no spherical aberration and high optical transmission at our operating wavelengths, these lenses provided the high optical performance we were looking for at low cost.

The size of the FOV depends on the available scanning range of the fiber tip and the overall magnification of the optical system. In turn, the extended fiber length determines the extent of tip deflection and the resonant frequency of the setup. We estimated a maximum fiber tip scan range of ± 250 μm for a 10-mm extended fiber length, ensuring the tip deflection could safely be accomplished using low voltages with minimal hysteresis. The fiber resonance frequency for the chosen 10-mm extended length was calculated to be at ~1 kHz, offering ablation speeds up to near 4 mm/s translational velocity for a 150 μm wide cut, as will be shown in the results. In a clinical setting, such speeds provide the ability for the surgeon to rapidly move the scalpel in one of the lateral directions without leaving unablated regions on the tissue.

The overall design of the scalpel is illustrated in Fig. 1 with the measured lateral and axial resolutions of the system. It consists of (1) a 7-μm, air-core PBF with mode field diameter (MDF) of 6 μm (NKT Photonics HC-800-02), (2) a piezoelectric tube actuator having a 3 mm outer diameter (Boston Piezo-Optics, PZT-5H) for fiber scanning, (3) an aspheric lens with 0.3 NA, 3.5 mm working distance, 3 mm outer diameter, and 2.8 mm clear aperture (Lightpath 354996 designed for 634 nm wavelength) for collimation of fiber output, and (4) an aspheric lens with 0.5 NA, 2 mm focal length, 3 mm outer diameter, and 2 mm clear aperture (Lightpath 352150 designed for 780 nm wavelength) for focusing on the tissue. To accommodate the tip deflection, we specifically investigated lenses having 3 mm diameter to match the diameter of our piezo tube, while providing largest clear aperture possible without increasing the device diameter further than that imposed by the piezo actuator. The housing wall thickness was designed to be ~1 mm to satisfy our overall diameter target of 5 mm, meanwhile providing a sturdy framework for the miniaturized components.

To select the optical components and estimate the expected device performance, we modeled the surgery beam pathway using ZEMAX optical design software. Figure 1(a) shows simulated rays, launched from the fiber tip at two different locations: blue line represents ray on the optical axis, red represents a ray at the edge of the clear aperture namely at the edge of the full scan range. Their centerline rays intersect with the optical axis at 1/3 of the fiber length away from the fiber fixation point, in other words 2/3 of the fiber length away from the

#206582 - $15.00 USD Received 18 Feb 2014; revised 23 May 2014; accepted 26 May 2014; published 2 Jun 2014

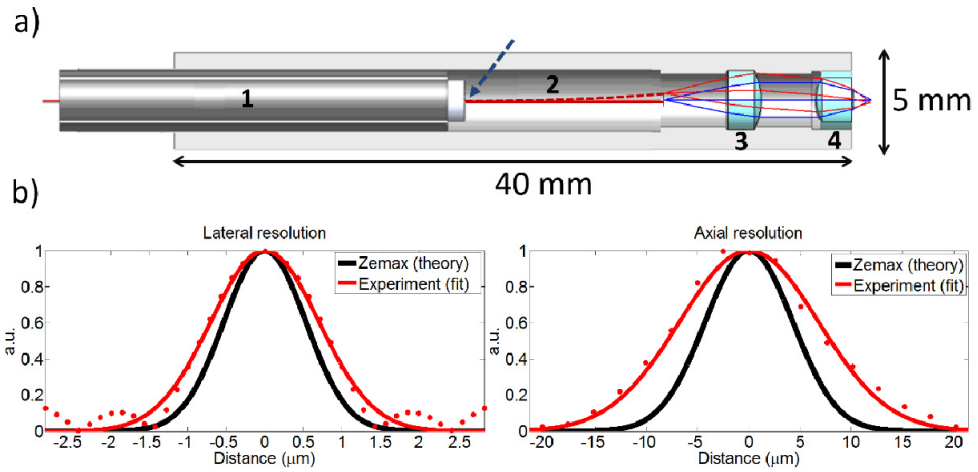

Fig. 1. Optical architecture and resolution of the scalpel. a) A computer assisted drawing (CAD) of the scalpel consisting of 1 – piezo actuator tube, 2 – air core PBF, 3 – collimation lens, and 4 – objective, as overlaid with ZEMAX ray tracing diagram. Blue arrow shows fiber fixation location. b) Measured and theoretical lateral and axial intensity distributions.

fiber tip, as dictated by cantilever bending formulation [19]. The beam divergence at the fiber tip, represented by two outer rays, is considered to be at the measured fiber NA of 0.17 (Fig. 2(a)).

Simulations showed that a collimation lens with 0.3 NA and over 2 mm clear aperture (Lightpath 354996) could accommodate a fiber tip deflection up to ± 250 μm without vignetting. Among the available high NA lenses, we chose a 0.5 NA lens (Lightpath 352150) as the focusing lens that could provide tight focusing over a square FOV of 220 μm x 220 μm for the maximum fiber tip deflection. Alternatively, we could choose a lens with a higher NA to achieve smaller spot size while compromising on the FOV and the working distance. Considering the curvature models of the lenses provided by the manufacturer, the ZEMAX simulation estimated the $1/e^2$ focused spot size to be 2.11 μm (Fig. 1(b)) at the optical axis with a Strehl ratio of 0.99. The aspheric lenses preserved the spot size during the scan, resulting in a Strehl ratio larger than 0.85 over the entire FOV. The radius of curvature of the FOV was 1.1 mm, mainly due to the fiber tip motion. This curvature corresponded to a ± 4 μm axial variation in the focal plane throughout the FOV from a planar surface. Furthermore, tolerance analysis on lenses and the fiber revealed that the resolution remained constant up to a 200 μm decenter and 2° tilt.

The housing was 40 mm long to hold all optical components in an in-line fashion. Its 5-mm outer diameter represents a near 50% reduction over our most recent MEMS-based endoscope with a 9.6 mm diameter [8]. The housing was 3-D printed via stereolithography technique, using DSM-Somos epoxy resin that mimics engineered plastics. With superior chemical resistance and broad heat and humidity tolerances, this material is a reliable and robust prototyping material for medical devices. The housing consisted of three grooves in which the rear side of the piezo tube and both lenses were press-fitted. Press-fitting allowed for simple assembly of the scalpel. However the lack of positioning control limited the ability to adjust component alignment that could partially be mitigated by testing a few housing iterations with different dimensions.

To fit the PBF inside the piezo tube actuator, we used a 23 gauge steel tubing to hold the PBF. Steel tubing was then inserted inside a polyethylene tubing with matching diameter to the piezo tube. After cleaving the fiber, we adjusted the extended length to approximately 11 mm and glued it to the steel tubing. Three electrical wires were soldiered to + x/+y electrodes

#206582 - $15.00 USD Received 18 Feb 2014; revised 23 May 2014; accepted 26 May 2014; published 2 Jun 2014

and ground terminals of the piezo tube for single sided actuation. Both piezo channels were connected to a signal generator through voltage amplifiers. We placed the objective, after adjusting the distance between the piezo tube and the collimation lens using a micro-manipulator to ensure collimation.

After assembling all micro-optical components and the piezo actuator tube within the housing, we coupled the laser beam into a ~1 meter long PBF using an underfilled 0.25 NA objective and a 5-axes stage (Newport, 561 series). The overall optical transmission of the system was 59% as a result of losses at fiber coupling and slight misalignment of optical components within the device that partially clipped the beam.

To characterize the resolution of the scalpel, we placed an external objective across the device and monitored the laser transmission using a photodetector while moving the United States Air Force (USAF) resolution chart across the focus. The resolution was deduced by focusing the beam from the device on to the USAF chart profile with a 2.2 μm line width, and by deconvolving the experimental data. The deconvolution was performed in the Fourier domain by dividing the Fourier transform of the acquired experimental data to that of the USAF chart profile. Rectangular windowing was performed in the frequency domain to suppress frequencies with high noise which led to small ringing artifact. We verified our resolution calculation by convolving an ideal Gaussian beam having equal width with that found from the deconvolution method and the USAF chart profile, which agreed well with the experimental data. These measurements matched well with knife-edge measurements within 2% difference.

At focus, the FWHM resolution was measured to be 1.64 ± 0.05 μm and 16.21 ± 0.05 μm in lateral and axial directions, respectively (Fig. 1(b)). The deduced resolutions reflect the mean and standard deviation for five different measurements. These resolutions correspond to intensity squared (two-photon) FWHM lateral and axial resolutions of 1.16 ± 0.04 μm and 11.46 ± 0.04 μm, respectively, showing a 10% improvement over our previous probe in both axes [8]. The resulting lateral $1/e^2$ intensity width was 2.8 ± 0.09 μm, which is essential in estimating the average laser fluence at the focal plane and defining fluence thresholds for ablation. The measured lateral and axial resolutions were 30% and 60% higher than their corresponding ZEMAX results. As expected, the axial resolution showed a higher difference between measured and simulated values due to its quadratic dependence on NA, as opposed to a linear dependence on NA for the lateral resolution. Despite having slightly poorer axial resolution than expected, ray simulations revealed that the collimating and focusing lens formed a powerful pair that could accommodate a FOV up to 220 μm x 220 μm without vignetting while maintaining near diffraction limited lateral resolution at all fiber scan angles.

2.2. Study of maximum pulse energy delivery through the air-core photonic bandgap fiber

The maximum energy that can be delivered using a single-mode, air-core PBF in our experimental conditions is expected to be limited by the ablation damage induced on the cladding by the tail of the propagating beam. This damage is likely to occur at the input face because of two general factors: 1) input energies are always higher than the output energies due to coupling efficiencies that are lower than 100% and/or transmission losses through the fiber and 2) even slight misalignments during coupling can cause the Gaussian beam to shift off the center slightly both laterally and axially and cause damage on the cladding at lower energies than the perfectly centered beams.

To increase the pulse energy that can be coupled into an air-core PBF, pre-chirping can be used to increase the pulse duration at the coupling while fiber dispersion can compress the pulse duration back to its original value at the fiber exit. Since the damage threshold of silica depends on the pulse duration and longer pulses cause damage at higher laser fluences, one can deliver higher pulse energies into the fiber by pre-chirping them to longer pulses. We previously observed an increase of more than 3 times in delivered energy by pre-chirping a 10 nm bandwidth, 120 fs laser pulse into a 3.8 ps pulse [7]. The pulse could then be chirped back

#206582 - $15.00 USD Received 18 Feb 2014; revised 23 May 2014; accepted 26 May 2014; published 2 Jun 2014

to near its original value as it propagated inside the fiber, experiencing negative dispersion. The limiting factor for maximum deliverable energies in this case was observed to be the damage at the input face of the 6 μm core size fiber. If a higher pre-chirping with a longer fiber was used or better coupling efficiencies could have been achieved, we could potentially deliver even higher pulse energies through the fiber. In that case, the ablation of the cladding could move somewhere along the fiber as the pulse compresses to shorter durations and increases its intensity. In the current study, however, the narrow bandwidth fiber-laser (3 nm) and the low dispersion of the fiber at the central laser wavelength, limited our pre-chirping capability.

There are other nonlinear mechanisms that can result in damaging the cladding and limit the maximum pulse energies deliverable through the PBFs. The high peak intensity of ultrafast laser pulses at the fiber core can induce a refractive index change in air due to the optical Kerr effect, arising from the third order nonlinear polarization. Varying index of refraction results in the phase modulation of the beam both temporally as well as spatially. The temporal phase modulation results in self-phase modulation (SPM) that broadens the spectra in PBFs and shortens the pulse as it propagates along the fiber. Reducing the pulse duration below its original value, SPM can cause the ablation of the cladding to occur along the fiber, as the damage threshold fluence of silica reduces due to reduced pulse widths. The spatial modulation of the index of refraction, on the other hand, may result in catastrophic self-focusing in the air-core of the fibers leading to air-breakdown. Both SPM and self-focusing can be mitigated by replacing the air in the fiber core with gases having smaller nonlinear refractive indices [14]. The air-breakdown threshold of $\sim 10^{14}$ W/cm^2 [20] corresponds to more than 50 μJ pulse energy for all of the focusing conditions used in our experiments. In our setup, air breakdown is unlikely to be experienced because the maximum pulse energies that can ideally be delivered through the 7-μm, air-core PBF is at least an order of magnitude smaller than this threshold. Therefore, we only considered the effect of SPM in our experiments.

To understand the maximum energy levels that could be delivered through the air-core PBF used in our miniaturized device, we therefore performed an in-depth study of the limiting parameters. Having eliminated the possibility of air breakdown in our experimental conditions, we focused on parameters effecting cladding damage and SPM. The cladding damage occurs when the fluence at the tail of the coupled beam right at the location of the cladding reaches the silica damage threshold. The laser fluence at the input facet cladding depends on the input pulse energy and the spot size and thus on the NA of the coupling lens, the diameter of the fiber core, as well as the profile of the focused beam. Moreover, system imperfections such as the pointing beam fluctuations and possible radial and axial misalignments during coupling can shift the focused beam and increase the laser fluence on the cladding at the fiber input face.

To study the NA effect on the maximum deliverable pulse energies, we tested three different coupling NA's of 0.18, 0.20, and 0.25 by over and under filling the back aperture of a 0.25 NA coupling lens (Fig. 2(a)). Different beam sizes at the back aperture was achieved by moving the coupling lens along the laser beam path. The measured spot sizes at the focal plane of the coupling lens were 6.2 ± 0.4 μm, 5.5 ± 0.2 μm, and 4.4 ± 0.4 μm, respectively (Fig. 2(b)). For each NA, we measured the maximum energy that could be delivered before a damage occurred at fiber input (Figs. 2(d) and 2(e)), as we did not observe any damage at the fiber output. During experiments, we defined fiber damage when the coupling efficiency dropped down by 20% of its maximum value. We successfully coupled maximum energies of 600 nJ, 765 nJ, and 850 nJ into the fiber with the corresponding output energies of 505 nJ, 705 nJ, and 660 nJ for NA`s of 0.18, 0.20, and 0.25, respectively. These data points represent the average of three measurements performed at each NA with error bars representing the corresponding standard deviation. The highest coupling efficiency of more than 92% was observed for NA = 0.20, where the focused spot size of 5.5 μm best matched the fiber MFD

#206582 - $15.00 USD Received 18 Feb 2014; revised 23 May 2014; accepted 26 May 2014; published 2 Jun 2014

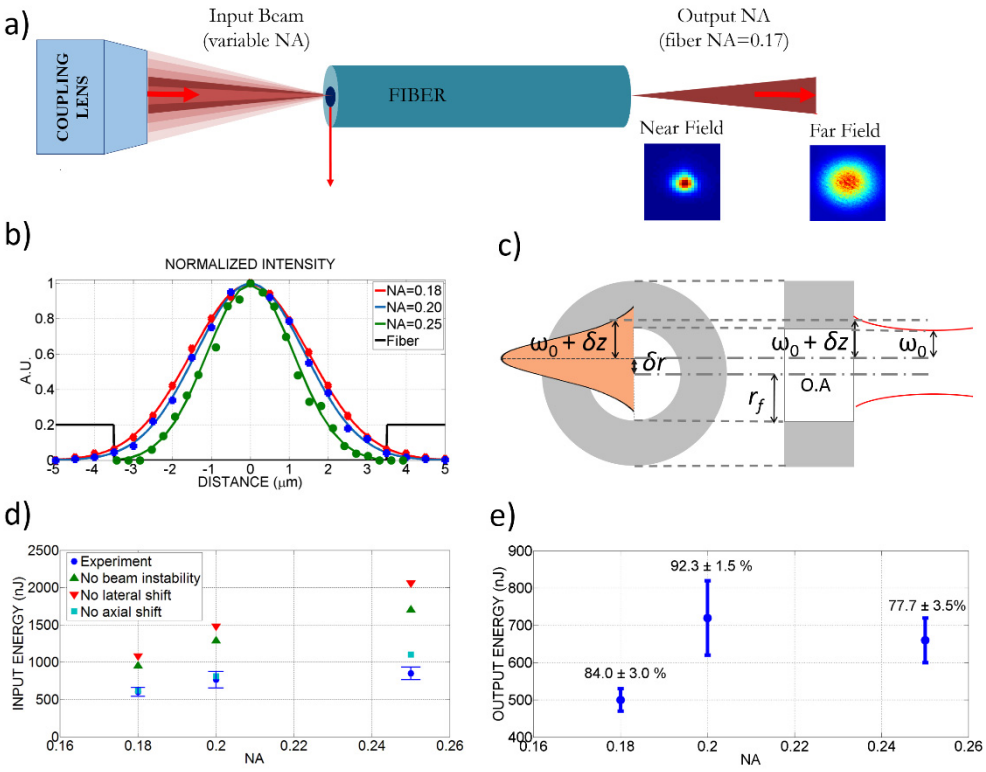

Fig. 2. Effect of coupling NA, coupling misalignments, and beam pointing instabilities on delivered energy through the 7-μm, air-core PBF. a) Simplified schematic of ultrashort pulse delivery through the PBF with various focusing conditions and measured near-field and far-field profiles at fiber output. b) Beam profiles at the focal point of the coupling lens as measured using the knife-edge test for different NA`s. c) Schematics illustrating the parameters for radial and axial coupling misalignments introduced in Eq. (1). d) Measured maximum input energies successfully coupled into the fiber for different coupling NA's and estimated maximum values assuming various misalignments during coupling. Error bars represent the standard deviation of three measurements performed at each NA. e) Measured output energies for each coupling NA with the coupling efficiencies above each data point as calculated based on the ratio of observed output energy to the input energy after coupling lens.

of 6 μm, as expected, delivering > 700 nJ laser energy at the fiber output. Coupling the laser at a higher NA enabled a higher input energy as the smaller laser spot size decreased the laser fluence interacting with the cladding. However, increasing the NA beyond the fiber`s NA resulted in a mismatch of not only NA but also MFD that reduced coupling efficiency and thus reduced delivered energies at the output as evident in Fig. 2(e).

To better analyze the measured fiber delivery parameters, we estimated the maximum achievable energy at the input facet assuming various imperfections during coupling did not exist. We specifically considered three possible system imperfections, the radial and axial misalignments of the coupled beam and pointing beam fluctuations inherent to the fiber laser. Radial misalignment and beam fluctuations would shift the focused beam location radially with respect to the optical axis of the fiber and axial misalignment will result in a larger beam size on the fiber input (Fig. 2(c)). As a result the laser fluence on the cladding will be increased for the same input energy. We therefore calculated the maximum pulse energies that could be delivered in the absence of each of these misalignments (Figs. 2(d) and 2(e)).

First, we measured pointing beam fluctuations of the laser by focusing it with a long focal length lens (f = 1 m) onto a high speed camera (VisionTech Phantom V series). By analyzing the beam profiles of 300,000 pulses (1 sec duration) that were collected every 10 minutes, we

#206582 - $15.00 USD Received 18 Feb 2014; revised 23 May 2014; accepted 26 May 2014; published 2 Jun 2014

could measure how the centroid of each individual pulse moved over time. We found the centroid of each spot by first locating the maximum intensity in each image and then fitting a Gaussian curve for both x and y axis. We found that the centroid of the laser beam drifted in one direction continuously for the first 3 hours of operation. Once the drift ended, the centroid fluctuated in an elliptical shape, shifting ± 24 μm along the long axis. The corresponding lateral shift of the beam at the focus of the 0.25 NA coupling lens with a 16.5 mm focal length was ± 0.4 μm.

We then calculated the threshold fluence at the tail of the beam on the cladding region (at $r = r_f$) for each coupling NA in the presence of estimated system imperfections. Assuming an ideal Gaussian beam distribution, the radial distribution of laser fluence is:

$$F(r) = \frac{2E}{\pi(w_0 + \delta z)^2} \exp\left(-2\left(\frac{r - \delta r}{w_0 + \delta z} \right)^2 \right) \text{thus; } F_{th} = F\left(r = r_f\right), \qquad (1)$$

where F_{th} is the damage threshold of the silica fiber cladding, E is the observed maximum input energy at the fiber input face, w_0 is the measured radius of the beam waist for each NA (Fig. 2(b)), r is the radial distance, r_f is the fiber core radius as measured to be 3.5 μm from SEM images in accordance with fiber specifications, δr is the total radial shift due to radial misalignments and beam fluctuations, and δz is the increase in spot size due to axial misalignments (Fig. 2(c)). In our system, the lateral misalignment was assumed to be due to the sensitivity of the fine adjustment knobs of the fiber alignment stage (0.5 μm) and the measured beam pointing fluctuations (0.4 μm). The resulting δr became 0.9 μm. As for the axial misalignment of the beam, we assumed ± 10 μm axial misalignment corresponding to half of the Rayleigh range of the coupling lens at 0.25 NA. The axial misalignment resulted in an increased beam size away from the beam waist in accordance with Gaussian beam formulation [21].

Taking these three imperfections into account, the damage thresholds were calculated to be similar for each NA as expected: 0.99 ± 0.03, 1.15 ± 0.05, and 0.97 ± 0.1 J/cm^2 for NAs of 0.18, 0.20, and 0.25, respectively. These calculated damage thresholds are indeed close to that of silica, which happens to be in the range of 1.5 – 2 J/cm^2 [22]. We attributed the difference in our observed damage threshold as opposed to the bulk silica damage threshold to a combination of various effects, such as the incubation effect [23], possibly larger radial and axial misalignments during coupling than the presumed values, surface roughness [24] of the input facet of the fiber that may result in hot spots, as well as deviations of our beam profile from an ideal Gaussian beam.

With the calculated damage thresholds, we then projected the laser energy that could be coupled into the fiber by excluding one system imperfection at a time based on Eq. (1). Radial misalignments during coupling and the pointing beam instabilities were identified as the most crucial factors potentially reducing the amount of the maximum deliverable pulse energies significantly, before a damage in the fiber could occur. As illustrated in Fig. 2(d), in the absence of radial misalignment (lateral shift) alone, for example, we would have been able to couple about 2 μJ energy into the fiber.

To test the severity of SPM in our setup, we performed a set of experiments where we measured pulse width and spectral range for various input energies throughout a 20 cm fiber. For pulse energies in the 500 nJ range, the pulse duration decreased from 1.5 ps to 1.41 ps. Based on our measurements at various energy levels, we deduced the nonlinear index of refraction of air (n_2) to be 2.7 × 10^{23} m^2/W using the formulation of change in spectral bandwidth with respect to pulse energy due to SPM [25]. Our findings were in close agreement with the measurements by Ouzounov *et al.*, where they found n_2 = 3 × 10^{23} m^2/W [26]. Using the measured nonlinear refractive index, a pulse width of 0.93 ps is estimated for

#206582 - $15.00 USD Received 18 Feb 2014; revised 23 May 2014; accepted 26 May 2014; published 2 Jun 2014

the 1-m long fiber used in the scalpel. Although such shortening of pulse width would result in slight decrease of damage threshold, the beam instability and misalignment effects, highlighted earlier, were highly critical and dominant over the SPM in limiting the amount of delivered pulse energies through the 7-μm, air-core PBF. Therefore, we expected the damage of the fiber cladding to occur at the input facet, as opposed to a damage along the fiber due to shortening of pulse width.

The theoretical upper bound for the coupled energy was calculated to be 3.3 μJ by neglecting all three imperfections simultaneously at the optimal NA. According to the coupling efficiency of 92.5%, a maximum energy of 3.05 μJ could be delivered at fiber output. Although the input facet can withstand higher energies with a higher NA due to reduced spot size and thus lowered fluence at the cladding, the tightly focused spot will quickly match the fiber MFD as it couples, which will actually limit the coupled energy. We may therefore argue that the maximum energy calculated for optimal NA that matches MFD under perfect conditions serves as an upper bound for input energy, namely, slightly above 3 μJ deliverable energy given that the pulse duration of 1.5 ps is preserved. However, the theoretical maximum input energy of 3.3 μJ would create significant SPM, reducing the pulse width to 300 fs at the end of 1-m fiber. In this case, SPM would become dominant in damaging the fiber cladding over the damage caused due to the beam instability and misalignment effects. Considering 1.5 times lowered damage threshold at 300 fs as compared to 1.5 ps, the fiber will actually get damaged at near 2.2 μJ as opposed to 3.3 μJ input energy. SPM would therefore set the ultimate limit on the deliverable energy through the fiber to approximately 2 μJ.

2.3. High speed ablation by resonant scanning

The ablation speed of our scalpel depends on fiber actuation dynamics and the repetition rate of the laser. To characterize the fiber actuation dynamics, we measured the resonance frequency of each axis and the resultant FOV for different applied peak voltages. The resonance frequency of the fiber depends on material properties of the fiber (Young`s modulus and density) and its geometry (radius and extended length) [19]. By sweeping the frequency of the sinusoidal driving voltage while imaging the fiber tip deflection using a CCD camera, we measured the resonance frequencies to be 895 Hz and 904 Hz for the x and y axes, respectively. These frequencies were in close agreement with the theoretical value of 900 Hz that would be expected for the measured extended fiber length of 11 mm. Minor cross coupling between the axes were observed due to the close values of x and y resonance frequencies and also due to the off-centered position of the fiber with respect to the central axis of the piezo tube. Driving one axis at resonance resulted in the actuation of the orthogonal axis by an amount that was roughly seven times smaller in amplitude.

To characterize the size of the FOV, we imaged the scanned area at the focal volume onto a CCD camera for various peak voltages applied to both axes simultaneously at their resonance frequencies. A peak voltage of 20 volts, for example, created a scan area of 150 μm × 150 μm. This low voltage not only provides safe use of such laser scalpel within human body, but also enables the use of simple operational amplifiers that can reduce cost and complexity of the driving electronics. Through driving all four electrodes, where –x and –y electrodes are phase reversed as opposed to + x and + y electrodes, the FOV can further be enlarged [27].

The successful implementation of ultrashort laser microsurgery in a clinic setting requires two essential parameters to be realized: 1) fast ablation speeds, so that the surgeon can move the FOV at clinically convenient speeds while achieving a continuous ablation and 2) a uniform ablation pattern that requires an equal number of overlapping pulses per spot over the entire FOV. To measure the speed and observe the pattern of ablation, we deposited a thin layer of gold on a cover glass and placed it at the focal plane of the device. Since the ablation threshold of gold is lower than that of the glass, we could tune the pulse energy to ablate only

#206582 - $15.00 USD Received 18 Feb 2014; revised 23 May 2014; accepted 26 May 2014; published 2 Jun 2014

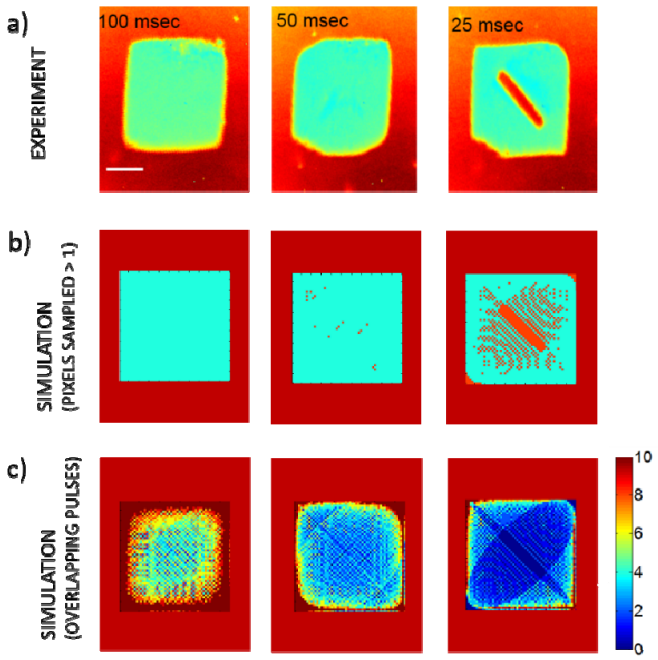

Fig. 3. Ablation patterns at various laser exposure durations. a) Optical microscopy images of ablated gold film on glass slide for durations of 100 ms, 50 ms, and 25 ms. b) Simulated Lissajous patterns for all three durations within the experimental FOV of 150 μm × 150 μm, where pixels sampled at least once were marked in green and unsampled pixels were marked in orange. c) Simulation results indicating the number of overlapping pulses at each pixel. Scale bar is 50 μm.

the gold film. This method enabled us to observe the direct signature of the ablation pattern and the size of the FOV for different laser exposure times.

Figure 3(a) presents optical images of the ablation pattern created on a 30 nm thick gold film on a glass sample for 100, 50, and 25 ms exposure times. We used pulse energies of 10 nJ, corresponding to an average fluence of 0.16 J/cm^2. This fluence level was expected to be sufficient to remove the thin gold layer with a single pulse. To estimate the ablation pattern, we simulated the expected Lissajous pattern within a 150 μm × 150 μm FOV, by taking into account fiber actuation resonance frequencies and pulse repetition rate. We considered the measured 1/e^2 spot size of 2.8 μm as the pixel size. Figure 3(b) shows the simulated binary ablation patterns, where each pixel that is sampled (ablated) at least once is indicated in green. Figure 3(c) reveals how many times each pixel is sampled within the FOV. The results indicated that 100%, 99%, and 79% of the pixels could be sampled for 100, 50, and 25 ms ablation durations, respectively. The pattern created over 50 ms demonstrated the most uniform number of overlapping pulses per spot over the FOV except at the corners. The sinusoidal nature of the Lissajous scan increased dwell times at the corners. All three simulated patterns qualitatively matched well the experimental observations. The period of the stable Lissajous pattern, which is the largest common divisor of both frequencies, was 1 Hz. Despite slow frame rate for obtaining a repeating Lissajous pattern, nearly 100% of the ablation spots could be sampled at least once within only 50 ms when operating with a 300 kHz repetition rate laser. The corresponding frame rate of 20 Hz indicates the potential for high-speed ablation with a fast updating and non-repeating Lissajous pattern scanning opportunity [28]. Even with 25 ms ablation duration, only a small non-ablated area in the middle remained, showing a significant speed advantage for microsurgery. In this case also, the number of overlapping pulses were nearly uniform over the FOV with one or more pulses overlapping in more than 80% of the FOV.

#206582 - $15.00 USD Received 18 Feb 2014; revised 23 May 2014; accepted 26 May 2014; published 2 Jun 2014

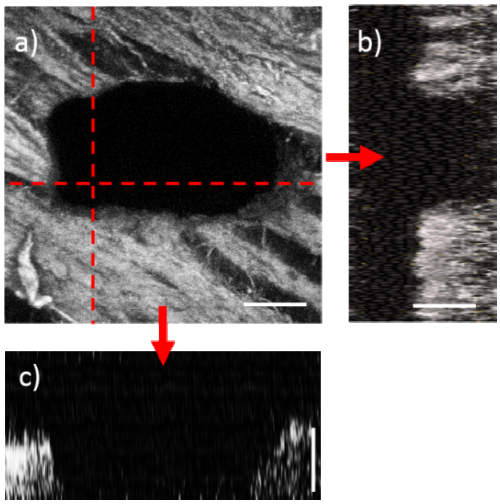

Fig. 4. Ablation of tissue surface using the 5-mm laser scalpel. (a) Nonlinear image of the laser drill through a 70 μm thick cheek pouch sample as revealed by the absence of the SHG signal from the collagen fibers. (b) The x-z cross section of the vertical dashed line shown in (a). (c) The y-z cross section of the horizontal line shown in (a). The cross sections illustrate through ablation across the tissue thickness. The laser pulse energies were 200 nJ, corresponding to average fluences of 3.2 J/cm^2. Scale bars are 50 μm.

To test the capability of our scalpel to ablate tissue, we performed microsurgery on the surface of fixed tissue slices of a scarred hamster cheek pouch sample. The cheek pouch tissues were prepared at Massachusetts General Hospital Voice Laboratory in Boston by Dr. James Kobler and shipped on dry ice to our laboratory. After delivery, the cheek pouches were stored at −80 °C. The details of this sample preparation are given in our previous publication [11]. The tissue was fixed by embedding into optimal cutting temperature compound, which provides a convenient specimen matrix for cryostat sectioning at temperatures below −10 °C. Fixation of the tissue allowed sectioning of the frozen tissue on a cryotome, which provided 70 μm thick tissue slices. For ablation experiments we have selected the slices below the epithelium where tissue collagen structure can be imaged using nonlinear imaging. Using 200 nJ pulse energies (average fluence of 3.2 J/cm^2), we were able to drill through a 70 μm thick slice within 10 seconds by moving the stage in the axial direction. Although fixed tissue was at room temperature during the experiment as opposed to body temperature that would be observed in a clinical setting, the difference in ablation thresholds between the two temperatures is negligible based on previous studies [29]. Prior to ablation, the surface was located by imaging the focused spot using a CCD camera. Once the surface was determined, we initiated the piezo-scanning with a targeted FOV of 150 μm × 150 μm and manually translated the device towards the tissue to accomplish the drill. The ablation was performed with the energy level (350 nJ at fiber input) that is less than half the energy that would damage the fiber at the coupling NA of 0.2. The coupling efficiency values measured before and after the ablation matched, indicating that there was no damage on the cladding.

Figure 4 illustrates second harmonic generation (SHG) images of the ablated tissue. We acquired these images using a benchtop nonlinear microscope following the ablation with the scalpel. The SHG signal originated at the collagen fibers and the loss of this signal indicated the ablated areas. The images clearly showed that we have successfully drilled through the thin slice of tissue by moving the scalpel's axial stage back and forth. The backlash of the manual stage and the slight oblique angle between the tissue and the optical axis, caused the ablated area to come out to be slightly different than what was targeted.

#206582 - $15.00 USD Received 18 Feb 2014; revised 23 May 2014; accepted 26 May 2014; published 2 Jun 2014

3. Discussion

In a surgical procedure, cutting speed varies greatly depending on the type of procedure, tissue, and the tool that is used for cutting. In general, applications that demand fast removal of non-fragile tissue such as bulk tumors, bones etc., benefit from high power lasers and mechanical removal tools. For instance, a high power CO_2 laser can ablate at great removal rates (>40 mm/s) [30] in the expense of significant collateral damage and a risk for carbonization. Mechanical cutting of tissue may also be performed at high speeds (~25 mm/s) [31], yet producing shear forces that results in a large border damage [32].

We estimated the tissue removal speed of our device through simulating a 2-D Lissajous pattern, with an additional linear translation term on one of the orthogonal directions in the lateral plane to model a tissue cut while translating the device at a constant speed (Fig. 5). We swept a number of velocity values till we achieved 100%, 90%, and 80% coverage within the ablated area. A translational speed of 2 mm/s allows the entire area to be ablated, where 100% of the pixels are sampled at least once. As we increased the translational speed to 3 mm/s and 3.7 mm/s, the percentage of pixels that are sampled at least once dropped down, as expected, to 90% and 80%, respectively. Such cutting speeds could still be adequate to tear the tissue. The ablation width of 150 μm matches the cut sizes achievable with mechanical scalpels and conventional CO_2 medical lasers having > 400 μm damage zone but with superior precisions in terms of the extent of the unwanted damage in the surrounding tissue [32].

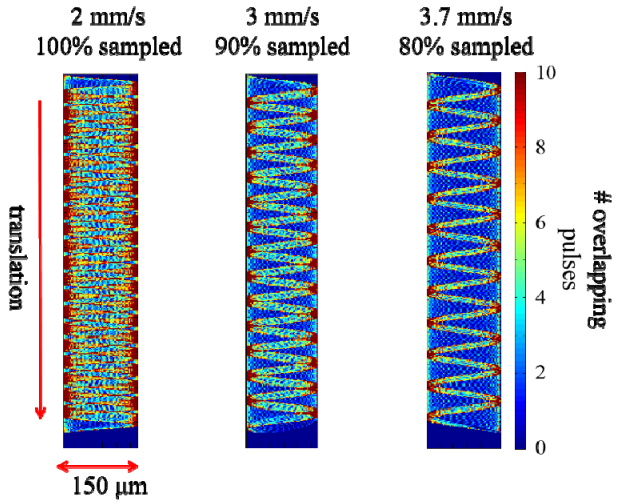

Fig. 5. Effect of translation speed on ablation coverage. Translational speed of 2 mm/s results in complete ablation while 3 mm/s and 3.7 m/s provide 90% and 80% coverage, respectively.

Challenges in bringing an ultrafast laser ablation device to clinic lie in the ability to improve the laser energy that can be delivered to the tissue while conserving the alignment of the laser to the fiber during the operation. Throughout this study, we used an off-the shelf, low-cost PBF fiber with relatively high NA, which could be converted into a large focusing NA at the tissue using a simple 2-lens optical design. Recent studies demonstrate transmission of high laser energies through novel large air-core Kagome fibers having low NA [13]. With further development, we aim to incorporate large air-core Kagome fibers to increase the amount of delivered energy for sub-epithelial ablation while utilizing smart optical designs to relay the low fiber NA to a high NA for focusing. However, when delivering higher pulse energies, one needs to be careful with SPM of the laser pulses that could potentially shift the damage along the fiber. We observed a slight narrowing of the pulse widths due to SPM in our experiments. However, the pointing beam instability and misalignment effects were more prominent than SPM and we observed damage at the input facet of our fiber.

#206582 - $15.00 USD Received 18 Feb 2014; revised 23 May 2014; accepted 26 May 2014; published 2 Jun 2014

Alignment of the laser in a clinical setting could be handled by a close-loop auto-alignment system. These systems are ideal for optimizing and maintaining free space coupling of a laser into a single mode fiber. Though such systems cannot compensate for rapid changes in pointing vector, it can overcome laser drift on the fiber due to other factors such as environmentally induced vibrations and temperature fluctuations. Additionally, misalignment in fiber coupling will be significantly mitigated, owing to the very fine adjustment sensitivity of the auto-alignment system in 3D.

The current device was designed as a surgery tool only, to remove tissues that can be located with visual inspection. Nevertheless, the device will eventually adopt various linear and nonlinear imaging modalities. With imaging capability, the device will be able to image in real-time, likewise our previous endoscope using a computer controlled data acquisition routine. The imaging capability will enable the clinician to rapidly locate the surface, epithelial, and sub-epithelial tissue layers via a manipulator on which the device is attached. Such a manipulator could either be controlled by the clinician or interfaced with haptic technology that converts the motion of the clinicians hand into micrometric movements of the device.

4. Conclusions

In this study, we developed a piezo-scanned fiber device for high speed ultrafast laser microsurgery, with an overall diameter of 5 mm. While the diameter of the scalpel is now half of our latest probe, its resolution has been also improved by 10% in both lateral and axial directions. The use of a high repetition rate fiber laser, delivering 300,000 pulses per second, and utilizing a sub-frame rate Lissajous scanning approach provided high ablation speeds suitable for clinical use. As shown by the uniform ablation of gold samples, an ablation FOV of 150 μm x 150 μm could be achieved within only 50 ms. With such ablation speeds, drilling into a cheek pouch tissue was possible using pulse energies of 200 nJ (3.2 J/cm^2). With these speeds the surgeon could potentially move the surgery probe at speeds near 4 mm/s laterally in one direction while continuously removing a 150 μm wide tissue layer.

With its improved resolution, smaller size, and surgical speed, our scalpel can be particularly useful for scarred vocal fold treatment, where we aim to create ablation voids to improve localization of injected biomaterials to restore vocal fold viscoelastisicity [11, 12]. Our laser scalpel can provide up to 450 nJ pulse energy, corresponding to 7.4 J/cm^2 fluence at the tissue. Having around 100 μm epithelial thickness [33], the complete ablation of sub-epithelial void in scarred human vocal folds will require fluences of more than 16 J/cm^2, higher than what this scalpel can deliver [11]. With its current ablative capability, the device would be useful in precisely dissecting around epithelial carcinoma sections. We were able to ablate a 70 μm deep trench, indicating that we could conveniently ablate greater depths by moving the device axially.

The major limitation in delivering higher pulse energies is identified to be the cladding damage at the input facet of the fiber. This limitation can potentially be mitigated by reducing the radial and axial misalignments, laser pointing beam fluctuations, and deviations of our beam profile from an ideal Gaussian beam. With the addition of imaging capability, our device can also serve as a useful tool for image-guided surgery in the oral cavity, larynx, colon, prostate, and open surgical sites.

Acknowledgments

The authors acknowledge the support from the National Science Foundation under grants BES-0548673, CBET-1014953, and Career Award (CBET-0846868), and a grant from the Cancer Prevention and Research Institute of Texas (CPRIT RP130412). We thank Raydiance Inc. for use of their Discovery fiber laser, and Dr. James Kobler from Massachusetts General Hospital for providing the tissue samples used in this study.

#206582 - $15.00 USD Received 18 Feb 2014; revised 23 May 2014; accepted 26 May 2014; published 2 Jun 2014